



Fe³⁺ doping promoted N₂ photofixation ability of honeycombed graphitic carbon nitride: The experimental and density functional theory simulation analysis

Shaozheng Hu^a, Xin Chen^a, Qiang Li^a, Fayun Li^a, Zhiping Fan^a, Hui Wang^a, Yanjuan Wang^a, Binghui Zheng^c, Guang Wu^{b,*}

^a College of Chemistry, Chemical Engineering, and Environmental Engineering, Liaoning Shihua University, Fushun 113001, China

^b School of Chemistry and Materials Sciences, Heilongjiang University, Harbin 150080, China

^c China Tianchen Engineering Corporation, Harbin, 150076, China

ARTICLE INFO

Article history:

Received 9 May 2016

Received in revised form 25 July 2016

Accepted 1 August 2016

Available online 2 August 2016

Keywords:

Graphitic carbon nitride

Honeycomb structure

Nitrogen photofixation

Fe³⁺ doping

DFT simulation

ABSTRACT

Honeycombed iron doped graphitic carbon nitride with outstanding N₂ photofixation ability is synthesized in this work. Characterization results indicate that Fe³⁺ inserts at the interstitial position and is stabilized in the electron-rich g-C₃N₄ through the coordinative Fe-N bonds. Fe³⁺ sites can chemisorb and activate N₂ molecules, then transfer the photogenerated electrons from the g-C₃N₄ to adsorbed N₂ molecules. Fe_{0.05}-CN displays the highest NH₄⁺ generation rate, which is approximately 13.5-fold higher than that of neat g-C₃N₄. Density functional theory simulations prove the N₂ activation effect of Fe³⁺ sites due to the high adsorption energy and prolonged N≡N bond. Charge density difference result confirms the electrons transfer process from the Fe³⁺ doping sites to N₂ molecule. DOS results indicate that the electrons of σ_g2p orbital (HOMO) in nitrogen atom is delocalized significantly when N₂ adsorbed on Fe³⁺ doping sites, leading to its orbital energy almost connects to that of π_g*2p orbital (LUMO), which confirming that Fe³⁺ doping sites can activate the N₂ molecule effectively. The Mulliken charge of nitrogen is −3.1 when the N₂ adsorbed on Fe³⁺ doping sites, indicating that N₂ molecule is enriched by large number of electrons, which is beneficial to the H⁺ attack to form NH₄⁺.

© 2016 Elsevier B.V. All rights reserved.

1. Introduction

Nitrogen is a necessary element of human, animal and plant growth. Although ~78% of the atmosphere is nitrogen, it is unusable directly to most organisms because of its strong nonpolar N≡N covalent triple bond. Thus, artificial nitrogen fixation is carried out through the Haber-Bosch process, in which hydrogen gas reacts with nitrogen gas to yield ammonia in the presence of catalysts under high pressure and temperature. Both the raw material costs and energy consumption are high for this process. Therefore, artificial nitrogen fixation under milder conditions is of great significance because of the reduction of input energy and no use of hydrogen. This significance has directed many chemists to find chemical [1,2], electrochemical [3,4] and photochemical routes [5,6] to fix nitrogen under mild conditions.

Nitrogen photofixation technology is considered to be a promising method to replace the traditional Haber-Bosch process. In 1977, the process of N₂ reduction to NH₃ over Fe doped TiO₂ was discovered by Schrauzer et al. [5]. Since then, many Ti-based semiconductor catalysts were reported [7–11]. However, because of the poor visible light absorption caused by the wide band gap energy, the nitrogen fixation abilities of these Ti-based semiconductor catalysts are still low under visible light. Moreover, the interfacial charge transfer efficiency of these semiconductor photocatalysts is far from satisfactory because of the poor interaction between catalyst and N₂ molecule [12–14]. Besides that, compared with the photocatalytic H₂ evolution and CO₂ reduction, photocatalytic N₂ fixation is more challenging because the N₂ fixation is seriously hampered by the high-energy N₂ intermediates in the reduced or protonated form (N₂[−] or N₂H) [15]. Thus, designing a new photocatalyst is not only important but also a challenge to develop the photocatalytic N₂ fixation technology. Against this background, in recent years, many novel nitrogen-fixation systems are reported successively [15–19]. Zhu et al. synthesized hydrogen-terminated diamond which can yield facile electron emission into

* Corresponding author.

E-mail address: guangwu001@163.com (G. Wu).

water, thus inducing photofixation of N_2 to NH_3 at ambient temperature and pressure [15]. Hu et al. prepared a novel ternary metal sulfide photocatalyst $\text{Zn}_{0.1}\text{Sn}_{0.1}\text{Cd}_{0.8}\text{S}$ with outstanding nitrogen photofixation ability under visible light [16]. Kitano et al. synthesized Ru-loaded $[\text{Ca}_{24}\text{Al}_{28}\text{O}_{64}]^{4+}(\text{e}^-)_4(\text{Ru}/\text{C12A7}:\text{e}^-)$. It has high electron-donating power, chemical stability and efficient ammonia synthesis performance [17]. Banerjee et al. prepared chalcogels containing FeMoS inorganic clusters, which are capable of photochemically reducing N_2 to NH_3 under white light irradiation [18]. Li et al. synthesized BiOCl nanosheet. DFT theoretical calculation results show that the fixation of terminal end-on bound N_2 on the oxygen vacancies of BiOCl {001} facets follows an asymmetric distal mode by selectively generating NH_3 [19].

Graphitic carbon nitride ($\text{g-C}_3\text{N}_4$), a novel metal-free semiconductor material, has been widely applied in many fields, including photocatalysis [20,21], fuel cells [22,23], organic synthesis [24] and gas storage [25,26]. The versatile application of $\text{g-C}_3\text{N}_4$ is largely due to its unique physicochemical properties, such as moderate band gap energy, energy-storage capacity, gas-adsorption capacity and special optical properties. However, the disadvantage of $\text{g-C}_3\text{N}_4$ is as prominent as its shortcomings. First of all, the high recombination rate of electrons and holes causes the low quantum efficiency. Secondly, a low surface area of $\text{g-C}_3\text{N}_4$ ($\sim 10 \text{ m}^2 \text{ g}^{-1}$) leads to the poor adsorption capacity of reactant and less active chemical sites.

Recently, Li et al. [27] reported oxygen vacancies introduced BiOBr nanosheet and Dong et al. [28] synthesized nitrogen vacancies doped $\text{g-C}_3\text{N}_4$. They suggested that, as the surface defects, oxygen vacancies and nitrogen vacancies could activate N_2 and promote interfacial electron transfer, leading to the improved N_2 photofixation ability. We hypothesize that, as another surface defects, the doping ions could have a similar effect on nitrogen photofixation. Owing to that Fe^{3+} doping can improve the nitrogen photofixation ability of TiO_2 based catalysts, in this work, honeycombed Fe^{3+} doped graphitic carbon nitride with outstanding nitrogen photofixation performance under visible light was prepared. On the one hand, Fe^{3+} doping can effectively trap the photogenerated electrons to improve the separation rate [29–31]. On the other hand, by controlling the Fe^{3+} concentration, honeycomb structure was obtained which significantly improved the surface area of as-prepared catalysts. The experimental and DFT calculation results indicate that Fe^{3+} doping sites can not only chemisorb and activate the N_2 molecule, but also promote interfacial electron transfer from catalysts to N_2 molecules, thus significantly improving the nitrogen photofixation ability.

2. Experimental

2.1. Preparation and characterization

All the chemicals used in this experiment were reagent grade and without further treatment. 4 g of melamine was dissolved into 60 mL of methanol at 60°C and stirred for 10 min. Then, 100 mL of HNO_3 (0.2 M) was added dropwise into above solution and the white precipitation was separated out. After cooling to room temperature, the white precipitate was collected, washed by methanol for three times and dried at 60°C for 12 h. Desired amount of $\text{Fe}(\text{NO}_3)_3 \cdot 9\text{H}_2\text{O}$ and the obtained white precipitate were added into 30 mL of methanol under stirring. The obtained suspension was heated to 50°C for evaporating methanol. The solid was dried at 60°C for 12 h, ground and calcined at 550°C for 2 h under flowing high purity argon gas at the rate of 5°C min^{-1} . The obtained sample was denoted as Fex-CN , where x stands for the mass ratio of $\text{Fe}(\text{NO}_3)_3 \cdot 9\text{H}_2\text{O}$ to melamine. For comparison, neat $\text{g-C}_3\text{N}_4$ was prepared following the same procedure mentioned above in the absence of $\text{Fe}(\text{NO}_3)_3 \cdot 9\text{H}_2\text{O}$ and denoted as FeO-CN .

The XRD patterns of the prepared samples were recorded on a Rigaku D/max-2400 instrument using $\text{Cu-K}\alpha$ radiation ($\lambda = 1.54 \text{ \AA}$). The scan rate, step size, voltage and current were $0.05^\circ/\text{min}$, 0.01° , 40 kV and 30 mA, respectively. UV–vis spectroscopy was carried out on a JASCO V-550 model UV–vis spectrophotometer using BaSO_4 as the reflectance sample. The morphologies of prepared catalyst were observed by using a scanning electron microscope (SEM, JSM 5600LV, JEOL Ltd.). Nitrogen adsorption was measured at -196°C on a Micromeritics 2010 analyser. All the samples were degassed at 393 K prior to the measurement. The BET surface area (S_{BET}) was calculated based on the adsorption isotherm. Thermogravimetric analysis (TGA) was performed using a TGA-DSC 2 (Mettler-Toledo) instrument. ICP was performed on a Perkin-Elmer Optima 3300DV apparatus. The XPS measurements were performed on a Thermo Escalab 250 XPS system with $\text{Al K}\alpha$ radiation as the excitation source. The binding energies were calibrated by referencing the C 1s peak (284.6 eV) to reduce the sample charge effect. Temperature Programmed Desorption (TPD) studies were performed using a CHEMBET-3000 (Quantachrome, U.S.A.) instrument in the temperature range of 313–1073 K. The photoluminescence (PL) spectra were measured at room temperature with a fluorospectrophotometer (FP-6300) using a Xe lamp as the excitation source. The photocurrents were measured using an electrochemical analyzer (CHI 618C Instruments) equipped with a rectangular-shaped quartz reactor ($20 \times 40 \times 50 \text{ mm}$) using a standard three-electrode system. The prepared sample film was used as the working electrode, a Pt flake was used as the counter electrode, and Ag/AgCl was used as the reference electrode. A 500 W Xe lamp was used to irradiate the working electrode from the back side. The light intensity on the working electrode was 120 mW cm^{-2} . In addition, a mechanical shutter was used to minimize the exposure of the sample to light. A 1.0 M Na_2SO_4 solution was used as the electrolyte. The applied potential was 0.00 V vs. Ag/AgCl . All the measurements were performed at room temperature (298 K).

Isotopic labeling experiments are carried out as follow. Labeled $^{15}\text{N}_2$ gas was purchased from Sigma-Aldrich Chemical Company. In the experimental process, Ar was used to eliminate air and the possible adsorbed ammonia in the reaction system. Then, $^{15}\text{N}_2$ was passed through the reaction mixture for 30 min. After that, the reactor was sealed. Other experiment conditions were the same as those for $^{14}\text{N}_2$ photofixation. Indophenol method was used to examine the produced $^{15}\text{NH}_4^+$, owing to the low mass of $^{15}\text{NH}_4^+$ for LC–MS studies. The sample for LC–MS analysis was prepared as follows. 0.5 mL of the reaction reacted with 0.1 mL of 1% phenolic solution in 95% ethanol. Then, 0.375 mL of 1% NaClO solution and 0.5 mL of 0.5% sodium nitroprusside solution were added into above solution. MS studies were carried on an Ultimate 3000-TSQ (LCMS-ESI).

The DFT simulations were performed using the program package Dmol3. The substrate is modelled by one layer of $\text{g-C}_3\text{N}_4$ separated by a vacuum layer of 12 Å. All the atoms in the layer and the N_2 molecule are allowed to relax. The Brillouin zones of the supercells were sampled by the Gamma points. Based on the structures of $\text{g-C}_3\text{N}_4$, the $\text{g-C}_3\text{N}_4$ surface with nitrogen atom vacancy was modelled to study the N_2 adsorption properties.

2.2. Photocatalytic reaction

The nitrogen photofixation property was evaluated according to previous literature [11]. The nitrogen photofixation experiments were performed in a double-walled quartz reactor in air. For these experiments, 0.2 g of photocatalyst was added to a 500 mL 0.789 g/L ethanol as a hole scavenger [11]. The suspension was dispersed using an ultrasonicator for 10 min. During the photoreaction under visible light irradiation, the suspension was exposed to a 250 W high-pressure sodium lamp with main emission in the range of 400–800 nm, and N_2 was bubbled at 100 mL/min through the solu-

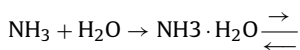
Table 1
Band gap, surface area, NH_4^+ generation rate ($r(\text{NH}_4^+)$) and Fe^{3+} concentration of as-prepared catalysts.

Sample	Band gap (eV)	S_{BET} (m^2g^{-1})	$r(\text{NH}_4^+)$ ($\text{mg}\cdot\text{L}^{-1}\cdot\text{h}^{-1}\cdot\text{g}_{\text{cat}}^{-1}$)	Fe^{3+} concentration (wt.%)	
				fresh	reused
Fe0-CN	2.59	7.7	0.40	0	0
Fe0.01-CN	2.55	8.4	2.57	0.32	0.30
Fe0.02-CN	2.52	12.5	3.05	0.55	0.57
Fe0.05-CN	2.50	45.5	5.40	1.31	1.34
Fe0.08-CN	2.47	25.6	3.97	1.84	1.77

tion. The UV light portion of the sodium lamp was filtered by a 0.5 M NaNO_2 solution. All runs were conducted at ambient pressure and 30 °C. At given time intervals, 5 mL aliquots of the suspension were collected and immediately centrifuged to separate the liquid samples from the solid catalyst. The concentration of ammonia was measured using the Nessler's reagent spectrophotometry method (JB7478-87) with a UV-2450 spectrophotometer (Shimadzu, Japan) [11,27].

3. Results and discussion

Fig. 1a shows the nitrogen photofixation performance over the as-prepared catalysts under visible light. The control experiment results indicate that the NH_4^+ generation rate can be ignored in the absence of irradiation, N_2 or photocatalyst, indicating that nitrogen photofixation occurs via a photocatalytic process. Fe0-CN shows the NH_4^+ generation rate ($r(\text{NH}_4^+)$) of $0.40 \text{ mg}\cdot\text{L}^{-1}\cdot\text{h}^{-1}\cdot\text{g}_{\text{cat}}^{-1}$. The $r(\text{NH}_4^+)$ for Fe^{3+} doped $\text{g-C}_3\text{N}_4$ obviously improves compared with Fe0-CN (Table 1). Fe0.05-CN displays the highest $r(\text{NH}_4^+)$, $5.40 \text{ mg}\cdot\text{L}^{-1}\cdot\text{h}^{-1}\cdot\text{g}_{\text{cat}}^{-1}$, which is approximately 13.5-fold higher than that of Fe0-CN. The Fig. 1a insert shows the photocatalytic stabilities of Fe0.05-CN. No obvious decrease in nitrogen photofixation ability is observed after 20 h, hinting its good stability. The Fe^{3+} concentrations of as-prepared catalysts were obtained by ICP (Table 1). No obvious difference between fresh and reused catalysts is shown, confirming the excellent structural stability. The addition of AgNO_3 as electron scavenger sharply suppresses the nitrogen photofixation ability of Fe0.05-CN (Fig. 1b), indicating the main active species is the photogenerated electron. No NH_4^+ is generated when using aprotic solvents (DMF and DMSO) instead of water, confirming that H_2O as the proton source is necessary for the nitrogen photofixation process (Fig. 1c). The change in the pH value of the Fe0.05-CN suspension during the nitrogen photofixation process is analyzed. Prior to the nitrogen photofixation process, the pH value of the suspension was measured to be 6.4. However, Fig. 1d shows that this pH value increases to 8.6 after 24 h because of the consumption of H^+ during the nitrogen photofixation process, as shown in the following equations:



In order to further investigate the nitrogen source of NH_4^+ , the N_2 photofixation ability of Fe0.05-CN under ^{15}N isotope-labeled N_2 (purity > 98%) was performed. The produced $^{15}\text{NH}_4^+$ reacts with phenolic and hypochlorite to form ^{15}N labeled indophenol, which was analyzed by LC-MS. A strong ^{15}N labeled indophenol anion mass spectroscopy signal presents at 199m/z in LC-MS studies (Fig. 1e). It is noted that this signal intensity is obviously higher than the ^{14}N : ^{15}N natural abundance ratio. This confirms that N_2 is the nitrogen source of generated NH_4^+ in this N_2 photofixation process. In order to compare the nitrogen photofixation ability with Ti-based catalysts, the Fe-TiO_2 , $\text{Fe}_2\text{Ti}_2\text{O}_7$ and Ru-TiO_2 were prepared according to the previous work [7,8,11]. The nitrogen photofixa-

tion abilities of prepared catalysts are shown in Fig. 1f. Obviously, Fe-TiO_2 and $\text{Fe}_2\text{Ti}_2\text{O}_7$ exhibit much lower nitrogen photofixation ability. The precious metal Ru doped TiO_2 shows the comparable nitrogen photofixation ability to that of Fe0.05-CN. However, considering the high price of precious metal, Fe0.05-CN is the best candidate among these catalysts.

Fig. 2a shows the XRD patterns of as-prepared catalysts. Two peaks at 13.1° and 27.3° are observed in all the catalysts, corresponding to (100) and (002) crystal planes of $\text{g-C}_3\text{N}_4$ [32]. No peak for Fe_2O_3 is observed, indicating Fe is not existed as oxide. This is consistent with previous results [29]. Whereas, an obvious shift toward a higher 2θ value is observed for all the Fe^{3+} doped $\text{g-C}_3\text{N}_4$ catalysts. This is probably due to the crystal lattice distortion which caused by the Fe^{3+} doping into $\text{g-C}_3\text{N}_4$ lattice. The light absorption property of as-prepared catalysts is studied by UV-vis spectra (Fig. 2b). $\text{g-C}_3\text{N}_4$ shows typical semiconductor absorption, originating from charge transfer response of $\text{g-C}_3\text{N}_4$ from the VB populated by N 2p orbital to the CB formed by C 2p orbital [33]. The obvious red shifts of absorption band are observed for all the Fe^{3+} doped $\text{g-C}_3\text{N}_4$ catalysts, indicating the band gap energies are decreased. This hints that Fe^{3+} doping could affect the electronic structure of $\text{g-C}_3\text{N}_4$, thus changes its optical property [29,34]. The band gaps are estimated from the tangent lines in the plots of the square root of the Kubelka-Munk functions against the photon energy (Fig. 2c) [35]. The result (Table 1) shows that the band gap decreases from 2.59 eV to 2.47 eV with increasing the Fe^{3+} concentration. In addition, it can be found that the volume of Fe0.05-CN with the same weight (0.1 g) is much larger than that of the Fe0-CN (Fig. 2b insert). This indicates that Fe0.05-CN is very fluffy and its specific surface area should be remarkably improved compared with Fe0-CN.

To characterize the specific surface area of $\text{g-C}_3\text{N}_4$ based catalysts, the nitrogen adsorption and desorption isotherms were measured (Fig. 2d). The isotherm all the as-prepared catalysts are of classical type IV, suggesting the presence of mesopores. The BET specific surface areas (S_{BET}) of Fe0-CN, Fe0.01-CN, Fe0.02-CN, Fe0.05-CN and Fe0.08-CN are calculated to be 7.7, 8.4, 12.5, 45.5 and $25.6 \text{ m}^2\cdot\text{g}^{-1}$ (Table 1). The S_{BET} increases firstly with increasing the Fe^{3+} concentration, then decreases for Fe0.08-CN. This is probably due to that Fe concentration strongly influences the morphology of catalysts. The large S_{BET} can promote adsorption, desorption and diffusion of reactants and products, which is favorable to the photocatalytic performance. The TGA result is shown in Fig. 2e. For Fe0-CN, the beginning temperature of the weight loss is approximately at 600 °C. The weight loss is 100% when the temperature rises to 750 °C, which is mainly attributed to the sublimation or decomposition of $\text{g-C}_3\text{N}_4$. For Fe0.05-CN, the similar weight loss curve is obtained, whereas 2.1 wt.% sample is remained. This remains should be Fe_2O_3 . According to this mass percentage of Fe_2O_3 , the Fe^{3+} content is approximately 1.5 wt.%, which is close to the ICP result (Table 1).

The morphologies of the representative samples were examined by using SEM analysis. Fig. 3a indicates that as-prepared Fe0-CN is composed of a large number of irregular particles. Those particles exhibit layer structure that is similar to its analogue graphite. The size of layered structure of Fe0.02-CN is obviously smaller than that

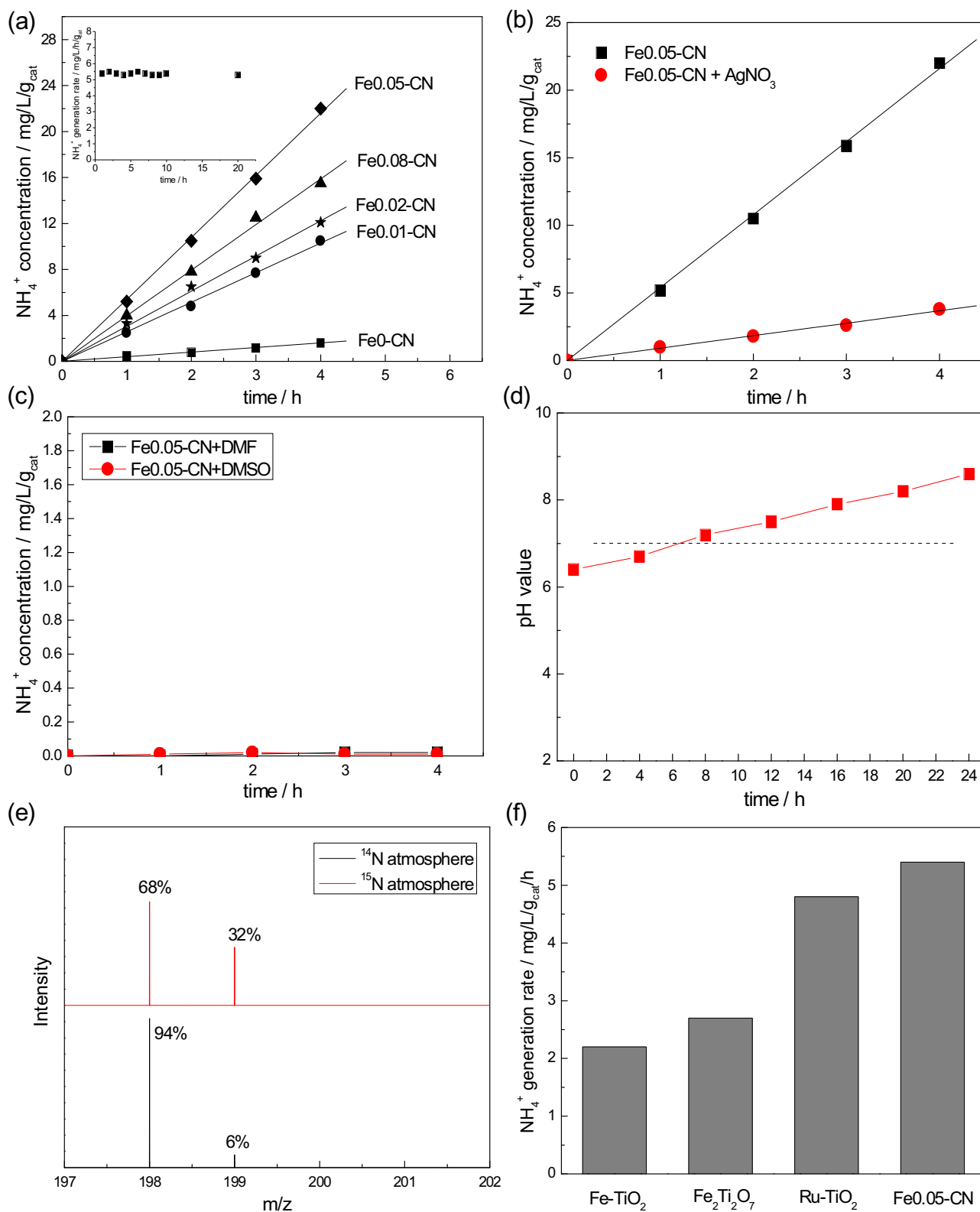


Fig. 1. The NH_4^+ production ability over as-prepared catalysts (a), NH_4^+ production ability of Fe0.05-CN using AgNO_3 as the electron scavenger (b) or in aprotic solvents DMF and DMSO (c), the pH value change of Fe0.05-CN suspension during the nitrogen photofixation process (d), the mass spectra of the indophenol prepared from different atmosphere (e) and the comparison of NH_4^+ production rate of Fe0.05-CN and Ti-based catalysts (f).

of Fe0-CN (Fig. 3b). This indicates that the low Fe^{3+} concentration could inhibit crystal growth of graphitic carbon nitride. For Fe0.05-CN (Fig. 3c, d), the honeycomb structure is obtained, accompanying with the formation of many irregular pores. Further increasing of

Fe^{3+} concentration causes the destruction of honeycomb structure (Fig. 3e). But these irregular pores are still observed on the surface of Fe0.08-CN. The elemental mapping images of Fe0.05-CN (Fig. 3f, g and h) indicate that Fe^{3+} is homogeneously distributed in the whole

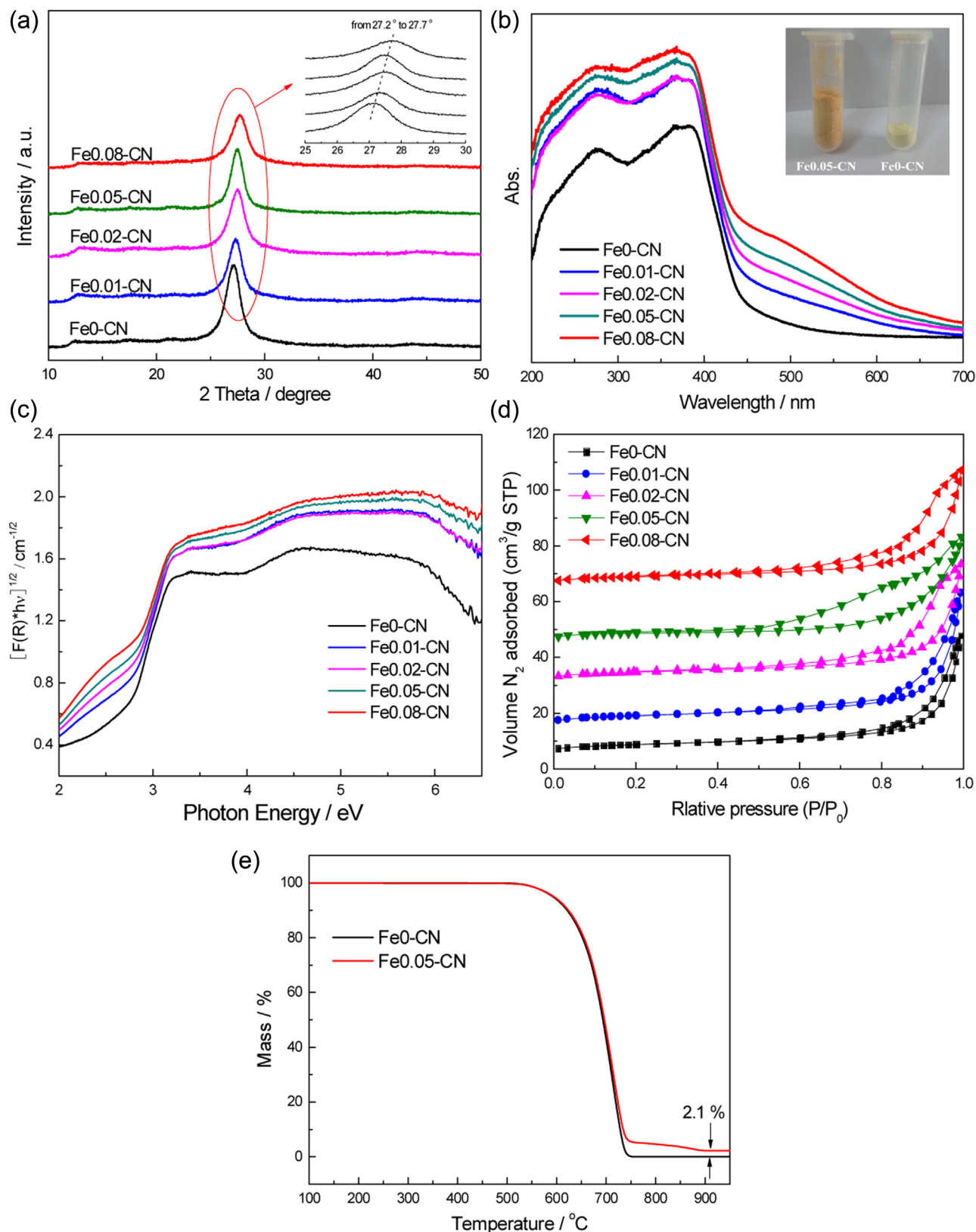


Fig. 2. XRD patterns (a), UV-vis spectra (b), Plots of the transformed Kubelka-Munk function versus the energy of light (c), N₂ adsorption-desorption isotherms (d) and TGA (e) of as-prepared catalysts.

host of g-C₃N₄. These results indicate that the Fe³⁺ concentration strongly influences the morphology of as-prepared g-C₃N₄ catalysts. Although the formation mechanism of this honeycombed

g-C₃N₄ is unclear till now, it is confirmed that both HNO₃ protonation [36] and doping treatment [37] can influence the morphology of as-prepared g-C₃N₄.

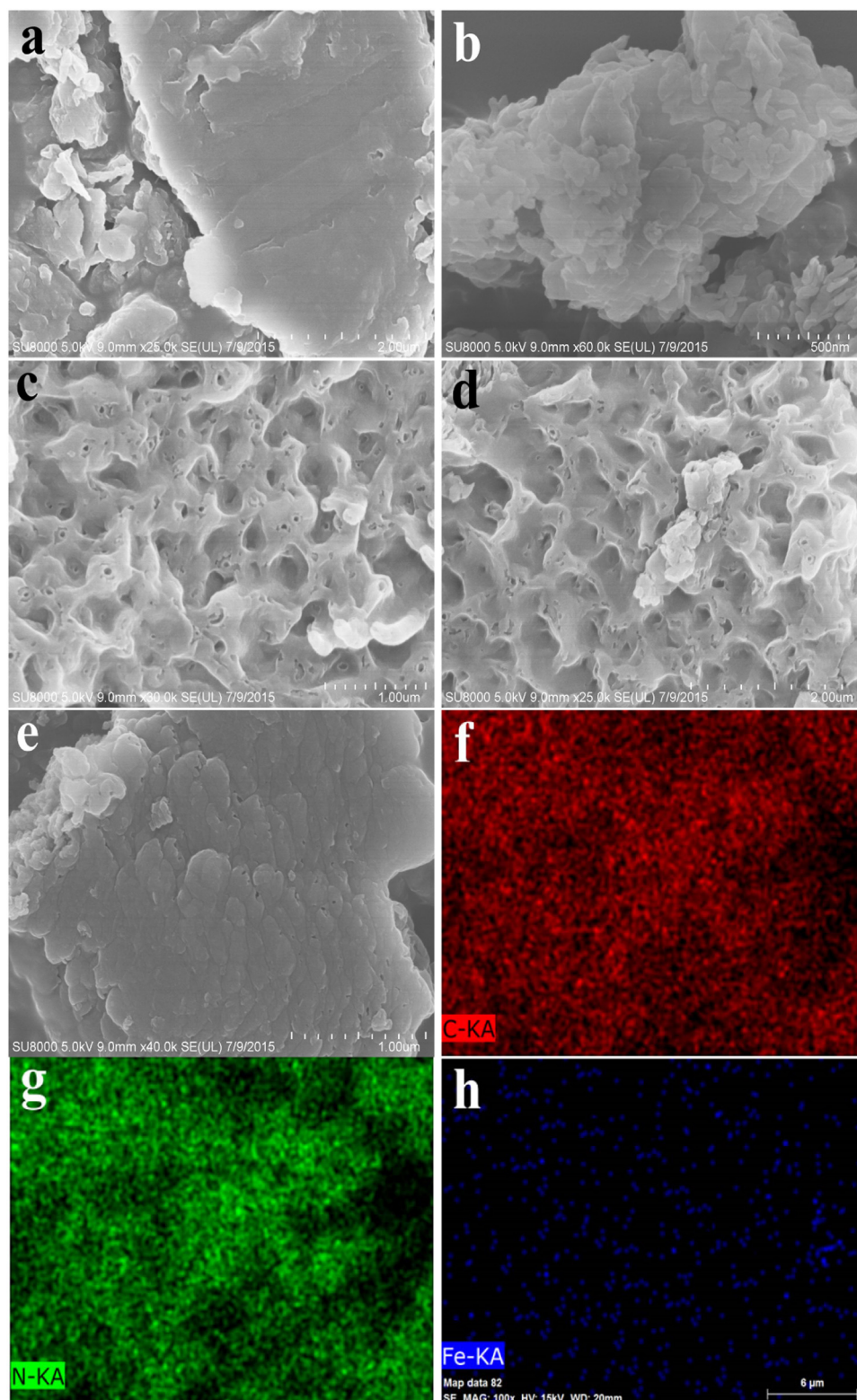


Fig. 3. SEM images of Fe0-CN (a), Fe0.02-CN (b), Fe0.05-CN (c, d), Fe0.08-CN (e) and elemental mapping images of Fe0.05-CN (f, g and h).

XPS of as prepared Fe0-CN and Fe0.05-CN are presented in Fig. 4. The spectra of Fe0-CN and Fe0.05-CN in both N 1s and C 1s region can be fitted with two contributions. In C 1s region (Fig. 4a), the peak with binding energy of 284.6 eV is attributed to the graphitic species in the CN matrix. The peak around 287.8 eV indicates the presence of sp^2 C atoms bonded to aliphatic amine ($-NH_2$ or $-NH-$)

in the aromatic rings [38,39]. In N 1s region (Fig. 4b), the main Ns peak with binding energy of 398.5 eV is assigned to sp^2 hybridized nitrogen ($C=N-C$), confirming the presence of sp^2 bonded graphitic carbon nitride. The peak at higher binding energy 400.9 eV is attributed to tertiary nitrogen ($N-(C)_3$) groups [40]. It is noted that, compared with Fe0-CN, an obvious shift to higher binding energy is

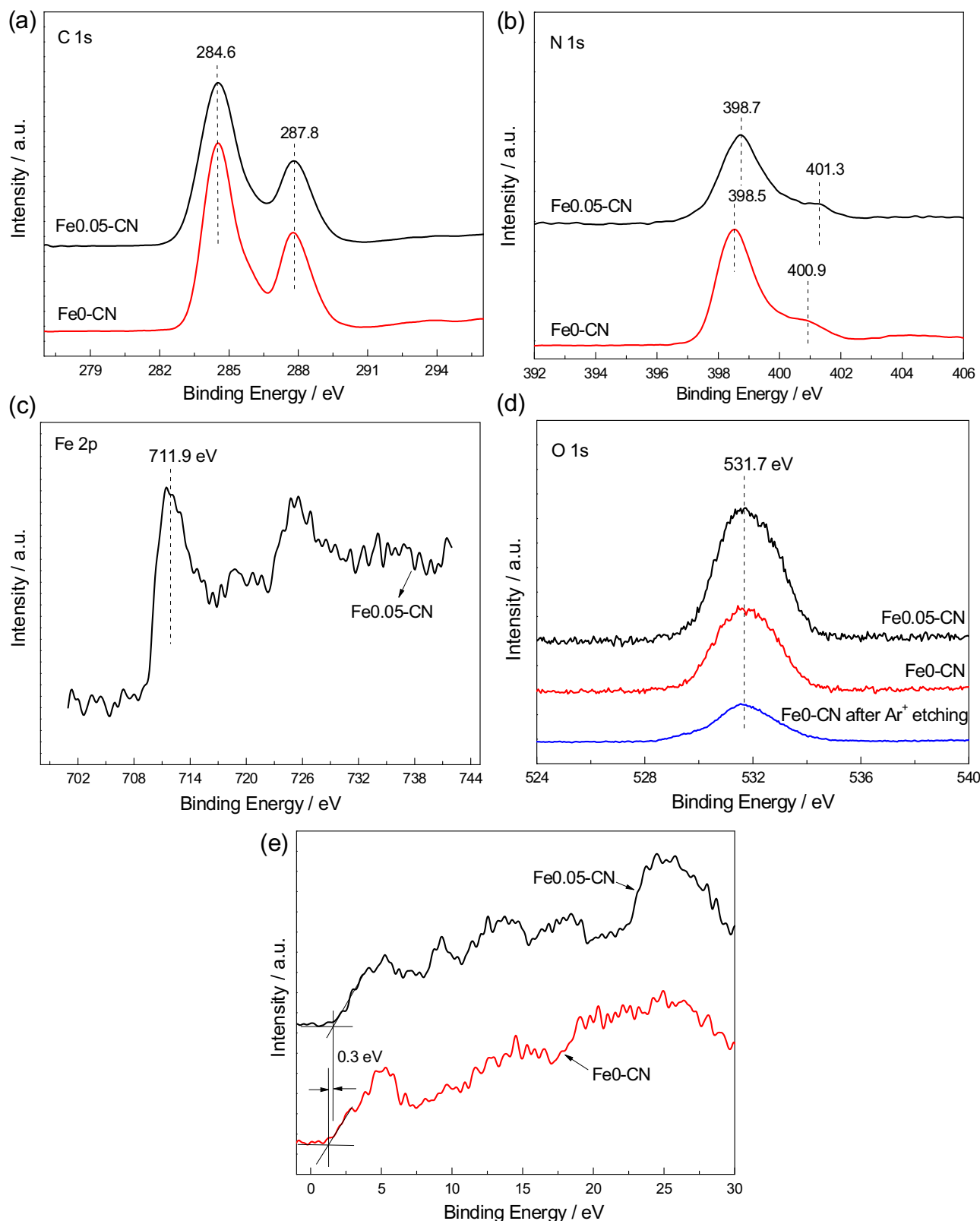


Fig. 4. XPS of as prepared Fe0.05-CN and Fe0-CN in the region of C 1s (a), N 1s (b), Fe 2p (c), O 1s (d) and VB XPS (e).

observed for Fe0.05-CN in the N 1s but not C 1s region. This is probably due to the change of chemical environment after Fe³⁺ doping. The electrons of the lone electron pair of nitrogen in g-C₃N₄ may be partially transferred to Fe³⁺ through the coordinative Fe-N bond, leading to the decreased electron density of nitrogen.

In Fig. 4c, the binding energy of Fe0.05-CN in Fe 2p region is located at 711.9 eV, obvious higher than the binding energies in the form of Fe₃O₄ and Fe₂O₃ [40,41]. This binding energy should be due to that Fe³⁺ inserts at the interstitial position and is stabilized in the electron-rich g-C₃N₄ structure through the coordinative Fe-N

covalent bonds, as reported by previous literatures [29,34,42]. This structure is similar to the metal organic complexes. In O 1s region (Fig. 4d), the peak with binding energy of 531.7 eV is observed for FeO-CN. As reported by previous literatures, this peak is assigned either to the adsorbed oxygen species [43–45] or to the N–C–O bond [46,47]. After Ar⁺ etching to eliminate the surface layer, this peak still exists, hinting it should be assigned to N–C–O bond. This oxygen is probably introduced during the synthesis process of catalyst. For FeO.05-CN, the peak area in the region of O 1s is larger than that of FeO-CN, indicating more oxygen exists in FeO.05-CN. However, no other oxygen species is observed in FeO.05-CN. This indicates the main existing form of oxygen is not iron oxide but N–C–O bond in FeO.05-CN. No peak for Fe₂O₃ is observed in XRD pattern, which is consistent with this result. The valence band XP spectra are shown in Fig. 4e. Compared with the spectrum of FeO-CN, an obvious shift is shown in FeO.05-CN, which should be attributed to the Fe³⁺ doped into g-C₃N₄ lattice. The E_{VB} is 1.26 and 1.56 eV for FeO-CN and FeO.05-CN, respectively. Combine with the UV–vis result, it is deduced that the E_{CB} for FeO-CN and FeO.05-CN is –1.33 and –0.94 eV. This band position indicates that the photogenerated electrons on FeO-CN should have the stronger N₂ reduction capability than that of FeO.05-CN. Thus it is deduced that the influence of Fe³⁺ doping on the band structure of g-C₃N₄ is not the main factor to enhance its N₂ photofixation ability.

Fig. 5a shows the PL spectra of as-prepared catalysts under N₂ atmosphere. In general, at a lower PL intensity, the separation rate of the photogenerated electron-hole pairs is higher [48]. A broad PL band around 470 nm which is observed for all the catalysts is attributed to the band-band PL phenomenon with the energy of light approximately equal to the band gap of g-C₃N₄. Such band-band PL signal is attributed to excitonic PL, which mainly results from the n- π^* electronic transitions involving lone pairs of nitrogen atoms in g-C₃N₄ [49]. The Fe³⁺ doped g-C₃N₄ catalysts show much lower PL intensities than that of FeO-CN. This indicates that Fe³⁺ doping is helpful for the separation of photogenerated electron-hole pairs. It is known that the reduction potential of Fe²⁺/Fe³⁺ is below the E_{CB} of g-C₃N₄ [34]. After Fe³⁺ doping, the photogenerated electrons could be trapped by Fe³⁺ doping sites, thus leading to the promoted separation rate of photogenerated electron-hole pairs. It is noted that the PL intensity decreases with increasing the Fe³⁺ concentration firstly, and then decreases for FeO.08-CN. Though the higher Fe³⁺ concentration of FeO.08-CN causes the more electron trapping sites, the honeycomb structure is destroyed under this Fe³⁺ concentration. The decreased surface area of FeO.08-CN causes that less electron trapping sites are exposed on the surface, leading to the reduced separation rate and nitrogen photofixation ability. Fig. 5b compares the PL intensity of FeO-CN and FeO.05-CN under Ar and N₂ atmospheres. The emission peak of FeO.05-CN is weaker than that of FeO-CN under both atmospheres, confirming that Fe³⁺ doping can act as electron trappers to improve carrier separation. Under N₂ atmosphere, the PL intensity of FeO.05-CN has been sharply reduced compared with that under an Ar atmosphere. By contrast, no obvious difference is observed for FeO-CN between the PL spectra under N₂ and Ar atmospheres. This suggests that Fe³⁺ doping may promote photogenerated electron transfer from as-prepared FeO.05-CN to adsorbed N₂.

Because the chemical adsorption sites are considered to be reaction centers to activate N₂ molecule, chemisorption is an essential step in photocatalytic N₂ fixation. N₂-TPD was carried out to investigate the N₂ adsorption situation on the surface of FeO-CN and FeO.05-CN (Fig. 6a). Obviously, two adsorbed N₂ species in FeO.05-CN are observed. One peak at ~110 °C is assigned to physical adsorption. The other peak at 280 °C is attributed to the strong chemisorption species of N₂ molecule. In the case of FeO-CN, only physical adsorbed N₂ species is observed. This result indicates that Fe³⁺ could act as chemical adsorption sites to activate

N₂ molecule for nitrogen photofixation. Thus the higher Fe³⁺ concentration causes the more chemical adsorption sites, leading to the higher nitrogen photofixation performance.

Fig. 6b shows the photocurrent responses of FeO-CN and FeO.05-CN under N₂ and Ar atmospheres. Because of the higher separation rate of electrons and holes, FeO.05-CN shows higher photocurrent than that of FeO-CN under both atmospheres. Note that the photocurrent generated on the FeO-CN electrode remains unchanged during irradiation time under both atmospheres. However, under N₂ atmosphere, the photocurrent density of FeO.05-CN gradually decreases at the beginning and then remains stable. This photocurrent decay is probably due to the electron capture competition existing between the N₂ and FTO glass. The photogenerated electrons which arrived at the surface of FeO.05-CN are trapped by the Fe³⁺ sites, and then transferred immediately from the catalyst to the adsorbed N₂, causing the photocurrent decay. In addition, the photocurrents of FeO-CN under N₂ and Ar atmospheres are almost the same. Whereas, the photocurrent of FeO.05-CN does not decay under Ar atmosphere. This result confirms that N₂ atmosphere is a necessary condition for this fast electron transfer process.

It is noted that the charges should be balanced in the as-prepared Fe³⁺ doped g-C₃N₄ catalysts. The oxygen in Fe³⁺ doped g-C₃N₄ could balance partial charges. But it is deduced from XPS and XRD results that the main existing form of oxygen is not iron oxide but N–C–O bond. Wang et al. considered that the charge of Fe³⁺ is mainly stabilized in the electron-rich g-C₃N₄ through Fe–N covalent bonds with only minor charge balance by Cl occurring [34]. In this work, we proposed the as-prepared Fe³⁺ doped g-C₃N₄ catalysts possess the similar structure with that reported by Wang but using oxygen instead of chlorine to balance partial charges [34]. In order to confirm our viewpoint, the neat Fe₂O₃ nanoparticles were prepared according to the previous work [50]. The Fe₂O₃/g-C₃N₄ composite was also prepared following the same procedure as in the synthesis of FeO.05-CN using Fe₂O₃ to replace Fe(NO₃)₃ · 9H₂O (with the same Fe content). The XPS results of neat Fe₂O₃, Fe₂O₃/g-C₃N₄ composite and FeO.05-CN in Fe 2p region are shown in Fig. 7a. Fe₂O₃/g-C₃N₄ composite and neat Fe₂O₃ show the peak with binding energy of 710.9 eV, which is assigned to the Fe³⁺ in the form of iron oxide [51]. For FeO.05-CN, the distinct binding energy shift of ~1 eV is observed. This confirms the existing form of Fe³⁺ in FeO.05-CN is not Fe₂O₃. The N₂ photofixation ability of Fe₂O₃/g-C₃N₄ composite is also compared with FeO-CN and FeO.05-CN (Fig. 7b). Obviously, Fe₂O₃/g-C₃N₄ composite shows almost the same N₂ photofixation ability as FeO-CN. This also confirms that the existing form of Fe³⁺ in FeO.05-CN is not the iron oxide. In addition, it is reported that the maximum in-planar distance of nitride pores is 0.71 nm [31,52], much larger than the radius of Fe³⁺ (~0.06 nm) [53,54]. Ghosh et al. calculated the properties of transition metal embedded graphitic carbon nitride using density functional theory. They also found that Fe interstitial doping occurs through Fe–N bonds [55]. Based on the characterization, reaction and calculation results mentioned above, it is concluded that Fe³⁺ does not exist as iron oxide but is mainly stabilized through Fe–N covalent bonds in the electron-rich g-C₃N₄.

To further investigate the interaction between a N₂ molecule and the Fe³⁺ doping sites, DFT simulations were carried out (Fig. 8). The optimized results indicate that the N₂ molecule prefers to adsorb on the Fe³⁺ doping sites. The adsorption energy is –134.8 kJ·mol^{–1}, confirming the chemisorption occurs. When the N₂ molecule interacts with Fe³⁺ doping sites, a coordinative Fe–N bond with the bond length of 1.82 Å forms. The N≡N bond activation over the Fe³⁺ doping sites can be reflected by the N≡N bond length increased to 1.181 Å, which is between the triple bond length (1.157 Å) of free N₂ molecular and the double bond length (1.201 Å) of diazene. However, only physical adsorption with the

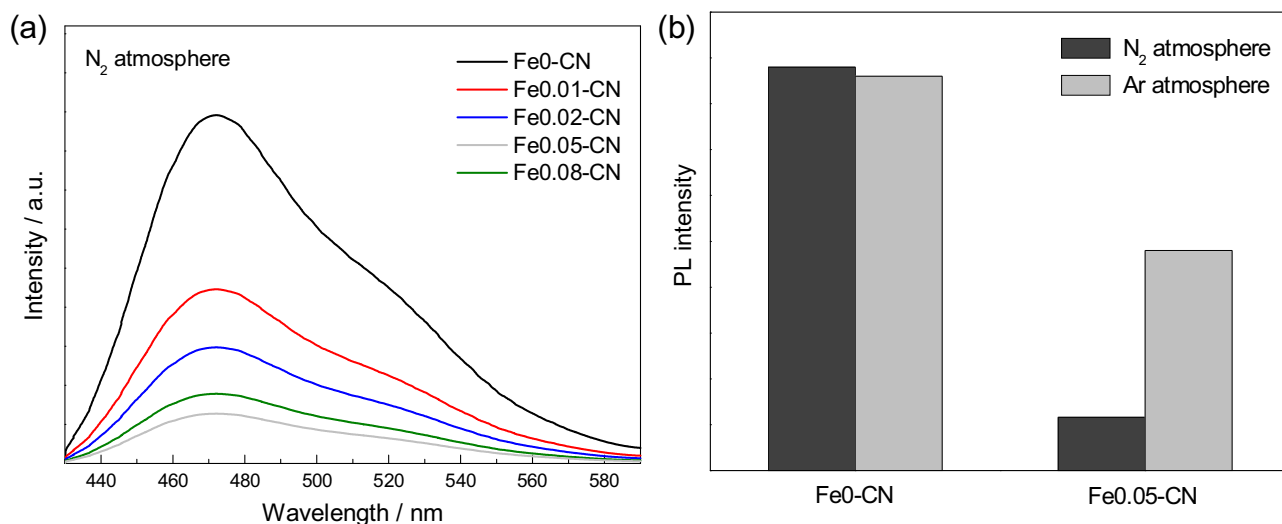


Fig. 5. PL spectra of as-prepared catalysts under N₂ atmospheres (a) and the comparison of PL intensity of Fe0-CN and Fe0.05-CN under Ar and N₂ atmospheres (b).

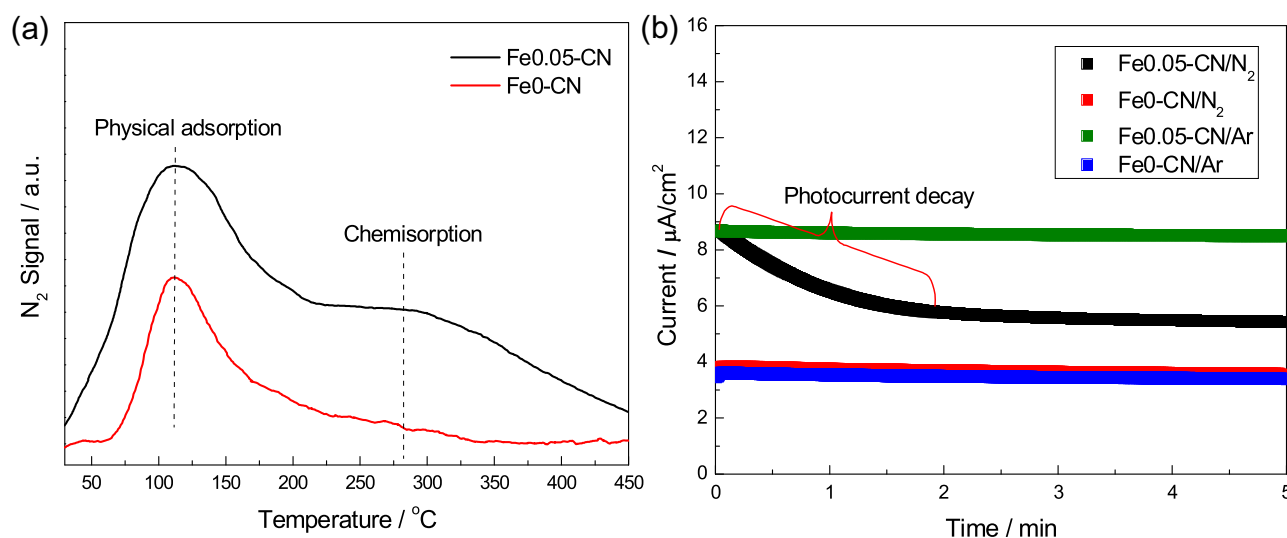


Fig. 6. N₂-TPD of Fe0-CN and Fe0.05-CN (a) and photocurrent responses of Fe0-CN and Fe0.05-CN under N₂ and Ar atmospheres (b).

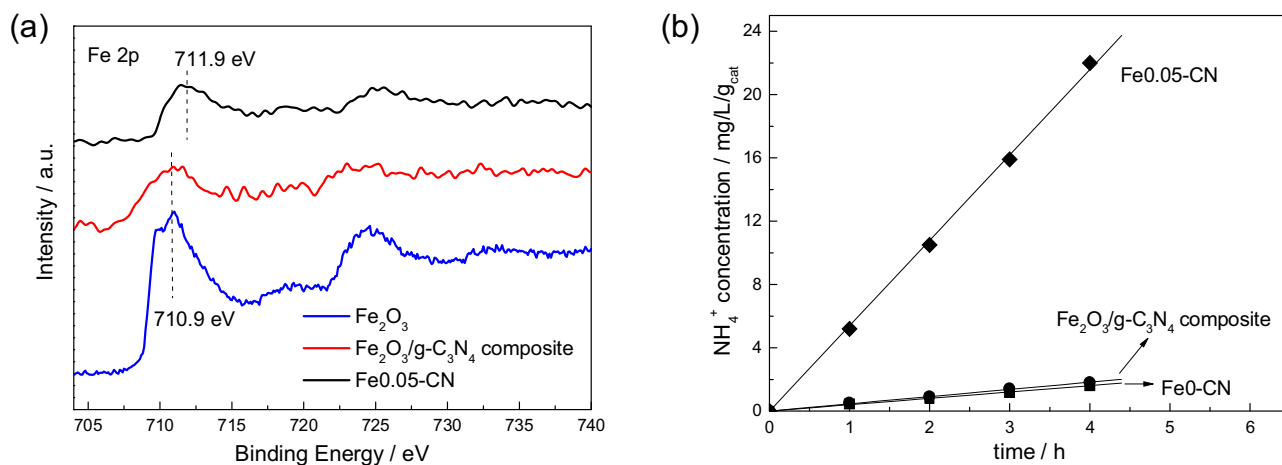


Fig. 7. XPS of neat Fe₂O₃, Fe₂O₃/g-C₃N₄ composite and Fe0.05-CN in Fe 2p region (a) and comparison of N₂ photofixation ability of Fe0-CN, Fe0.05-CN and Fe₂O₃/g-C₃N₄ composite (b).

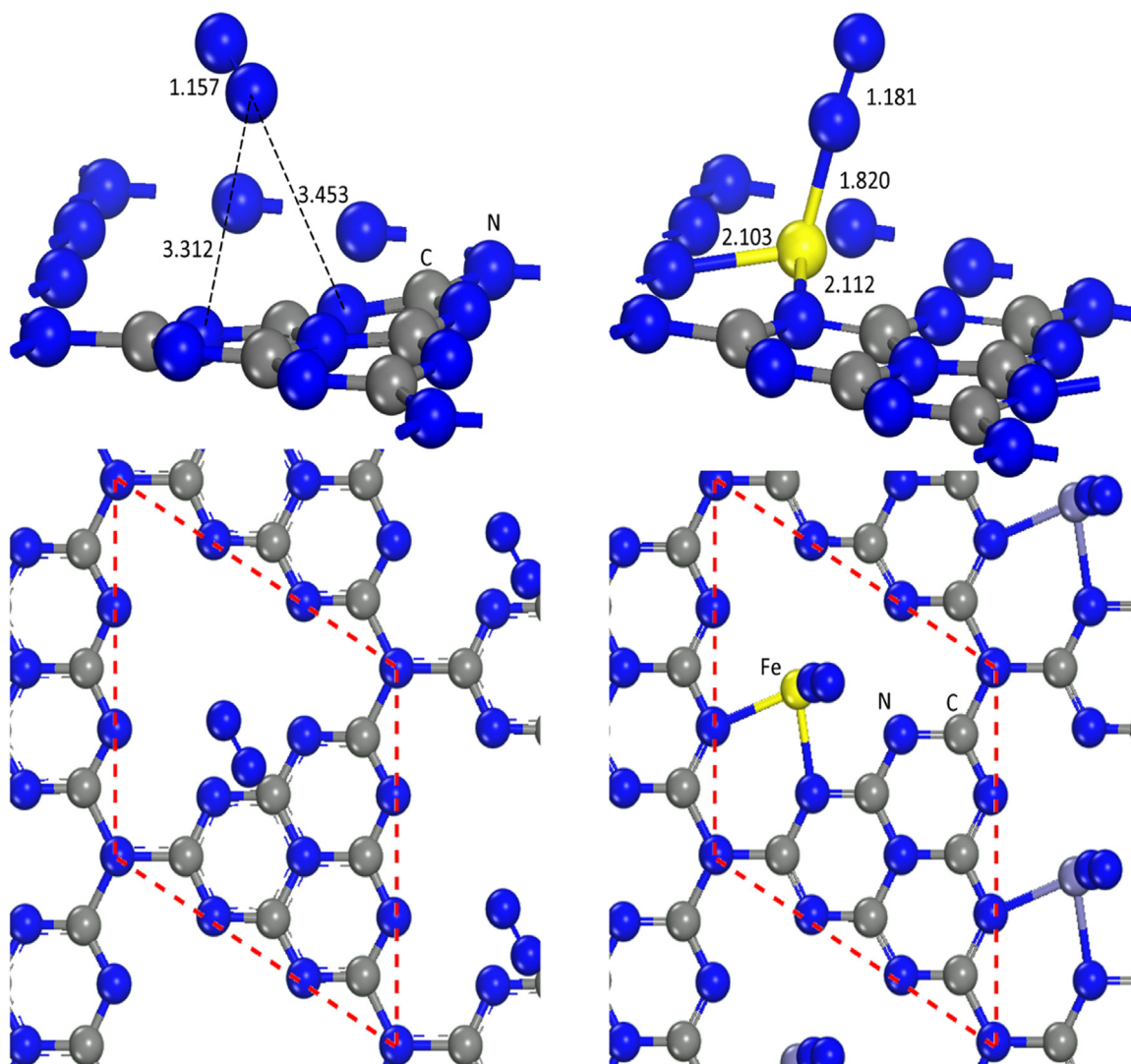


Fig. 8. The optimal N_2 adsorption models on Fe0-CN (left) and Fe0.05-CN (right).

adsorption energy of $-14.6 \text{ kJ}\cdot\text{mol}^{-1}$ occurs when N_2 is adsorbed on Fe0-CN. The distance between N_2 and Fe0-CN is much longer than that between N_2 and Fe0.05-CN. The $N\equiv N$ bond length is also not changed.

Charge density difference was carried out to simulate the electrons transfer behavior (Fig. 9). The result indicates that the exchange and transfer of electrons mainly take place between the Fe^{3+} doping sites and N_2 molecule. The obvious electrons transfer from the Fe^{3+} doping sites to N_2 molecule, as depicted by the electron depletion on Fe^{3+} doping sites and electron accumulation on the N_2 molecule, is observed. Such electron back-donation phenomenon is also found in transition metal- N_2 complexes, in which the transitional metals such as Fe, Mo and Co donate their available d-orbital electrons into the $N-N$ anti-bonding orbital to activate the ligand [27,56–58]. The activated N_2 could create molecular steps to form the high-energy intermediates ($-N_2^-$, $-N_2H$ or $HN=NH$) and finally produce the NH_4^+ via successive proton and electron transfer process [59].

Density of states (DOS) of s and p orbitals of free nitrogen molecule, nitrogen molecule adsorbed on Fe0-CN and Fe0.05-CN are shown in Fig. 10. For free nitrogen molecule, five peaks are observed. The peaks located at -17.85 , -3.80 , -1.23 , and 0.00 eV are assigned to $\sigma_g 2s$, $\sigma_u^* 2s$, $\pi_u 2p$, and $\sigma_g 2p$ orbitals, respectively. $\sigma_g 2p$ orbital is the highest occupied molecular orbital (HOMO). The

band range above the Fermi level (7.32 eV) is defined as the $\pi_g^* 2p$ orbital, which is the lowest unoccupied molecular orbital (LUMO). When N_2 interacted with Fe0-CN, the orbitals of nitrogen atom are not obviously changed compared with that in the absence of catalyst, hinting the poor N_2 activation ability of Fe0-CN. However, when N_2 adsorbed on Fe^{3+} doping sites, the electrons of $\sigma_g 2p$ orbital (HOMO) in nitrogen atom is delocalized significantly, leading to its orbital energy almost connects to that of $\pi_g^* 2p$ orbital (LUMO). This suggests that Fe0.05-CN can activate the N_2 molecule effectively. The Mulliken charge of nitrogen interacted with Fe0-CN is -0.1 , which is nearly the same as free nitrogen molecule. However, this value decreases to -3.1 when the N_2 adsorbed on Fe^{3+} doping sites, indicating that the N_2 molecule is enriched by large number of electrons. These electrons should be assigned to the photogenerated electrons transferred from the Fe^{3+} doping sites. This electron-rich environment is beneficial to the H^+ attack to form NH_4^+ .

4. Conclusions

Honeycombed iron doped graphitic carbon nitride with outstanding N_2 photofixation ability is synthesized in this work. The results show that Fe^{3+} inserts at the interstitial position and is stabilized in the electron-rich g- C_3N_4 structure through the coordinative Fe-N bonds. Fe^{3+} sites not only serve as active sites to adsorb and

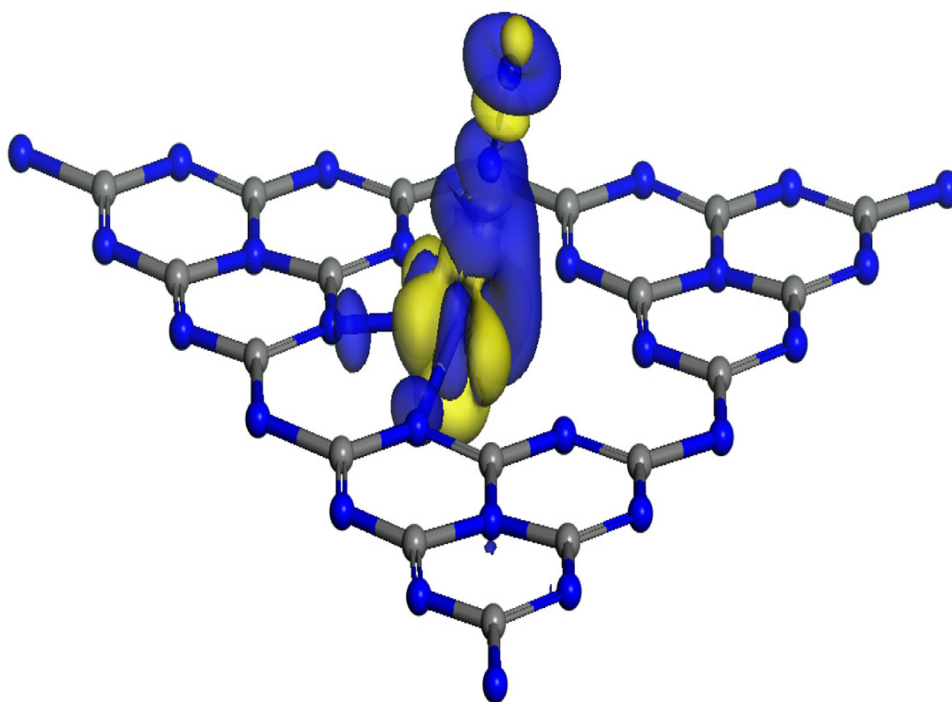


Fig. 9. The charge density difference of the N_2 molecule adsorbed on Fe^{3+} doping sites (The yellow and blue isosurfaces represent charge accumulation and depletion in the space, respectively). (For interpretation of the references to colour in this figure legend, the reader is referred to the web version of this article.)

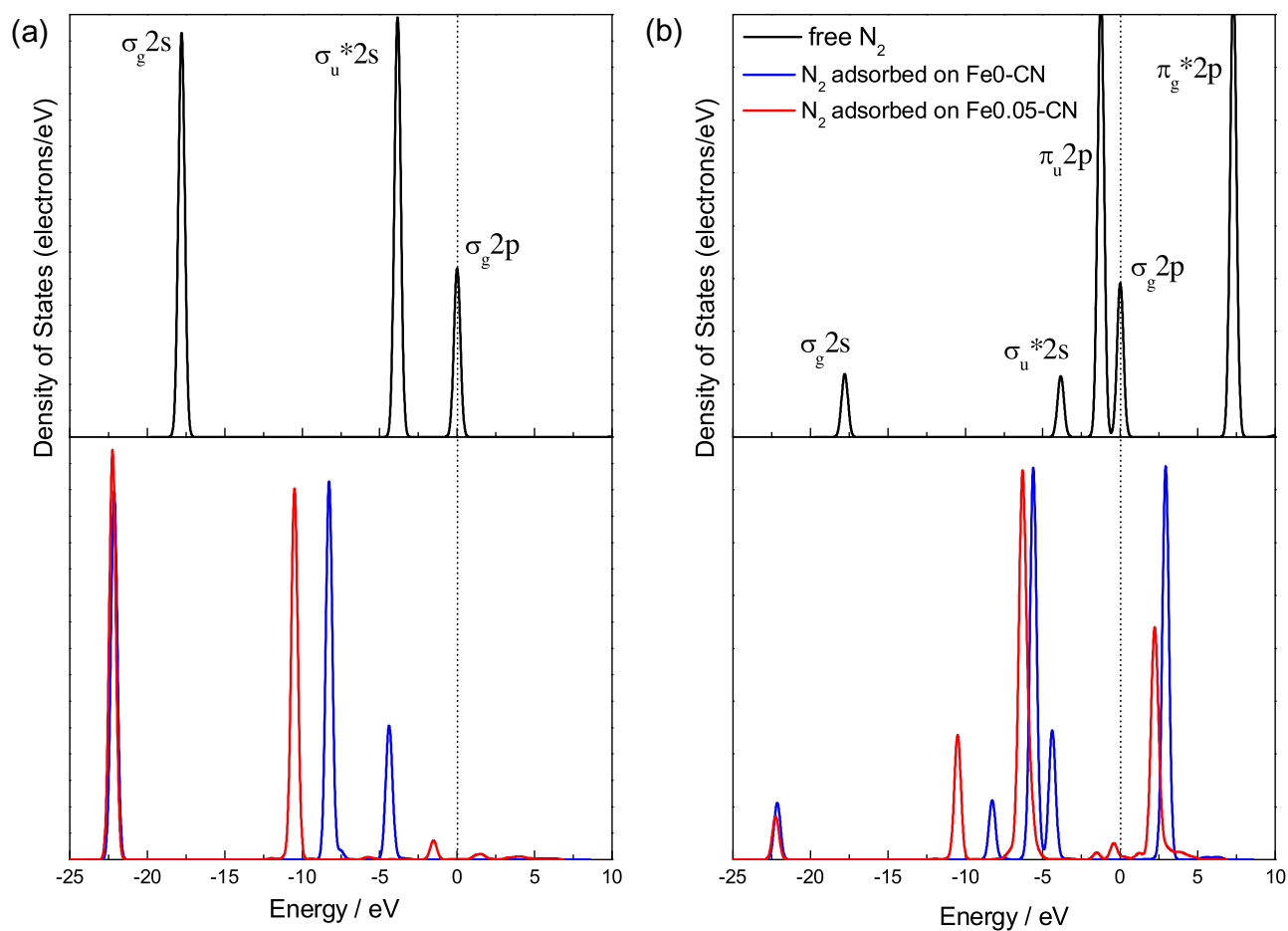


Fig. 10. Density of states of s (a) and p (b) orbitals of free nitrogen molecule, nitrogen molecule adsorbed on Fe0-CN and Fe0.05-CN.

activate N₂ molecules but also promote interfacial charge transfer from catalysts to N₂ molecules, thus significantly improving the nitrogen photofixation ability. The adsorption energy is $-134.8 \text{ kJ}\cdot\text{mol}^{-1}$ when N₂ molecule interacts with Fe³⁺ doping sites. The N≡N bond is prolonged from 1.157 Å to 1.181 Å, proving that Fe³⁺ doping sites can activate N₂ molecule. Charge density difference result confirms the electrons transfer process from the Fe³⁺ doping sites to N₂ molecule. The electrons of $\sigma_g 2p$ orbital (HOMO) in nitrogen atom is delocalized significantly when N₂ adsorbed on Fe³⁺ doping sites, leading to its orbital energy almost connects to that of $\pi_g^* 2p$ orbital (LUMO), which confirming that Fe³⁺ doping sites can activate the N₂ molecule effectively. The Mulliken charge of nitrogen is -3.1 when the N₂ adsorbed on Fe³⁺ doping sites. This indicates the N₂ molecule is enriched by large number of electrons, which is beneficial to the H⁺ attack to form NH₄⁺.

Acknowledgment

This work was supported by Science & Technology Research Foundation of Heilongjiang Province Education Bureau of China (No.12541626) and Postdoctoral Fund of Heilongjiang province of China (No. LBH-Z14208), Education Department of Liaoning Province (No. L2014145) and Environmental Science and Engineering Innovation Team of Liaoning Shihua University ([2014]-11).

References

- [1] M.E. Vol'pin, V.B. Shur, E.G. Berkovich, *Inorg. Chim. Acta.* 280 (1998) 264–274.
- [2] G.J. Leigh, *Science* 279 (1998) 506–507.
- [3] E.E. van Tamelen, B. Akerman, *J. Am. Chem. Soc.* 90 (1968) 4492–4493.
- [4] C.R. Dickson, A.J. Nozik, *J. Am. Chem. Soc.* 100 (1978) 8007–8009.
- [5] G.N. Schrauzer, T.D. Guth, *J. Am. Chem. Soc.* 99 (1977) 7189–7193.
- [6] K.T. Ranjit, B. Viswanathan, *Indian J. Chem. Sect. A* 35 (1996) 443–448.
- [7] K.T. Ranjit, T.K. Varadarajan, B. Viswanathan, *J. Photochem. Photobiol. A: Chem.* 96 (1996) 181–185.
- [8] O. Rusina, O. Linnik, A. Eremenko, H. Kisch, *Chem. Eur. J.* 9 (2003) 561–565.
- [9] K. Hoshino, *Chem. Eur. J.* 7 (2001) 2727–2731.
- [10] K. Hoshino, M. Inui, T. Kitamura, H. Kokado (Eds.), *Angew. Chem. Int.* 39 (2000) 2509–2512.
- [11] W.R. Zhao, J. Zhang, X. Zhu, M. Zhang, J. Tang, M. Tan, Y. Wang, *Appl. Catal. B: Environ.* 144 (2014) 468–477.
- [12] Y.T. Liang, B.K. Vijayan, K.A. Gray, M.C. Hersam, *Nano Lett.* 11 (2011) 2865–2870.
- [13] M.G. Walter, E.L. Warren, J.R. McKone, S.W. Boettcher, Q. Mi, E.A. Santori, N.S. Lewis, *Chem. Rev.* 110 (2010) 6446–6473.
- [14] P.J. Britto, K.S.V. Santhanam, A. Rubio, J.A. Alonso, P.M. Ajayan, *Adv. Mater.* 11 (1999) 154–157.
- [15] D. Zhu, L. Zhang, R.E. Ruther, R.J. Hamers, *Nat. Mater.* 12 (2013) 836–841.
- [16] S.Z. Hu, X. Chen, Q. Li, Y.F. Zhao, W. Mao, *Catal. Sci. Technol.* (2016), <http://dx.doi.org/10.1039/C6CY00622A>.
- [17] M. Kitano, Y. Inoue, Y. Yamazaki, F. Hayashi, S. Kanbara, S. Matsuishi, T. Yokoyama, S.W. Kim, M. Hara, H. Hosono, *Nat. Chem.* 4 (2012) 934–940.
- [18] A. Banerjee, B.D. Yuh, E.A. Margulies, Y.B. Zhang, Y. Shim, M.R. Wasielewski, M.G. Kanatzidis, *J. Am. Chem. Soc.* 137 (2015) 2030–2034.
- [19] H. Li, J. Shang, J.G. Shi, K. Zhao, L.Z. Zhang, *Nanoscale* 8 (2016) 1986–1993.
- [20] T. Xiong, W.L. Cen, Y.X. Zhang, F. Dong, *ACS Catal.* 6 (2016) 2462–2472.
- [21] F. Dong, Z.W. Zhao, Y.J. Sun, Y.X. Zhang, S. Yan, Z.B. Wu, *Environ. Sci. Tech.* 49 (2015) 12432–12440.
- [22] Y. Zheng, J. Liu, J. Liang, M. Jaroniec, S. Qiao, *Energy Environ. Sci.* 5 (2012) 6717–6731.
- [23] Y. Zheng, Y. Jiao, J. Chen, J. Liu, J. Liang, A. Du, W. Zhang, Z. Zhu, S.C. Smith, M. Jaroniec, G. Lu, S. Qiao, *J. Am. Chem. Soc.* 133 (2011) 20116–20119.
- [24] J. Xu, H.T. Wu, X. Wang, B. Xue, Y.X. Li, Y. Cao, *Phys. Chem. Chem. Phys.* 15 (2013) 4510–4517.
- [25] Q. Li, J. Yang, D. Feng, Z. Wu, Q. Wu, S.S. Park, C.S. Ha, D. Zhao, *Nano Res.* 3 (2010) 632–642.
- [26] S.S. Park, S.W. Chu, C. Xue, D. Zhao, C.S. Ha, *J. Mater. Chem.* 21 (2011) 10801–10807.
- [27] H. Li, J. Shang, Z.H. Ai, L.Z. Zhang, *J. Am. Chem. Soc.* 137 (2015) 6393–6399.
- [28] G.H. Dong, W.K. Ho, C.Y. Wang, *J. Mater. Chem. A* 3 (2015) 23435–23441.
- [29] X.F. Chen, J.S. Zhang, X.Z. Fu, M. Antonietti, X.C. Wang, *J. Am. Chem. Soc.* 131 (2009) 11658–11659.
- [30] S.Z. Hu, R.R. Jin, G. Lu, D. Liu, J.Z. Gui, *RSC Adv.* 4 (2014) 24863–24869.
- [31] Q. Li, L. Ma, J.G. You, F.Y. Li, Z.P. Fan, G. Lu, D. Liu, J.Z. Gui, *Appl. Surf. Sci.* 311 (2014) 164–171.
- [32] Y. Wang, X.C. Wang, M. Antonietti (Eds.), *Angew. Chem. Int.* 51 (2012) 68–89.
- [33] X.C. Wang, K. Maeda, A. Thomas, K. Takanabe, G. Xin, K. Domen, M. Antonietti, *Nat. Mater.* 8 (2009) 76–80.
- [34] X.C. Wang, X.F. Chen, A. Thomas, X.Z. Fu, M. Antonietti, *Adv. Mater.* 21 (2009) 1609–1612.
- [35] Y.I. Kim, S.J. Atherton, E.S. Brigham, T.E. Mallouk, *J. Phys. Chem.* 97 (1993) 11802–11810.
- [36] Y.J. Zhong, Z.Q. Wang, J.Y. Feng, S.C. Yan, H.T. Zhang, Z.S. Li, Z.G. Zou, *Appl. Surf. Sci.* 295 (2014) 253–259.
- [37] Y.P. Zhu, T.Z. Ren, Z.Y. Yuan, *ACS Appl. Mater. Interfaces* 7 (2015) 16850–16856.
- [38] L. Ge, C. Han, *Appl. Catal. B: Environ.* 117–118 (2012) 268–274.
- [39] W. Lei, D. Portehault, R. Dimova, M. Antonietti, *J. Am. Chem. Soc.* 133 (2011) 7121–7127.
- [40] Y.W. Zhang, J.H. Liu, G. Wu, W. Chen, *Nanoscale* 4 (2012) 5300–5303.
- [41] X.S. Zhou, B. Jin, R.Q. Chen, F. Peng, Y.P. Fang, *Mater. Res. Bull.* 48 (2013) 1447–1452.
- [42] F. Goettmann, A. Fischer, M. Antonietti, A. Thomas (Eds.), *Angew. Chem. Int.* 45 (2006) 4467–4471.
- [43] H. Xu, J. Yan, X.J. She, L. Xu, J.X. Xia, Y.G. Xu, Y.H. Song, L.Y. Huang, H.M. Li, *Nanoscale* 6 (2014) 1406–1415.
- [44] K.X. Li, L.S. Yan, Z.X. Zeng, S.L. Luo, X.B. Luo, X.M. Liu, H.Q. Guo, Y.H. Guo, *Appl. Catal. B: Environ.* 156–157 (2014) 141–152.
- [45] P. Niu, Y.Q. Yang, J.C. Yu, G. Liu, H.M. Cheng, *Chem. Commun.* 50 (2014) 10837–10840.
- [46] L.F. Ming, H. Yue, L.M. Xu, F. Chen, *J. Mater. Chem. A* 2 (2014) 19145–19149.
- [47] J.H. Li, B. Shen, Z.H. Hong, B.Z. Lin, B.F. Gao, Y.L. Chen, *Chem. Commun.* 48 (2012) 12017–12019.
- [48] S.Z. Hu, F.Y. Li, Z.P. Fan, F. Wang, Y.F. Zhao, Z.B. Lv, *Dalton Trans.* 44 (2015) 1084–1092.
- [49] V.N. Khabashesku, J.L. Zimmerman, J.L. Margrave, *Chem. Mater.* 12 (2000) 3264–3270.
- [50] A.K. Mondal, S.Q. Chen, D.W. Su, K. Kretschmer, H. Liu, G.X. Wang, *J. Alloys Comp.* 648 (2015) 732–739.
- [51] L. Xu, J.X. Xia, H. Xu, S. Yin, K. Wang, L.Y. Huang, L.G. Wang, H.M. Li, *J. Power Sources* 245 (2014) 866–874.
- [52] X.G. Ma, Y.H. Lv, J. Xu, Y.F. Liu, R.Q. Zhang, Y.F. Zhu, *J. Phys. Chem. C* 116 (2012) 23485–23493.
- [53] Z.J. Li, W.Z. Shen, W.S. He, X.T. Zu, J. Hazard. Mater. 155 (2008) 590–594.
- [54] S.Z. Hu, F.Y. Li, Z.P. Fan, C.C. Chang, *Appl. Surf. Sci.* 258 (2011) 182–188.
- [55] D. Ghosh, G. Periyasamy, B. Pandey, S.K. Pati, *J. Mater. Chem. C* 2 (2014) 7943–7951.
- [56] Y. Tanabe, Y. Nishibayashi, *Coord. Chem. Rev.* 257 (2013) 2551–2565.
- [57] H.P. Jia, E.A. Quadrelli, *Chem. Soc. Rev.* 43 (2014) 547–564.
- [58] C. Sivasankar, S. Baskaran, M. Tamizmani, K. Ramakrishna, *J. Organomet. Chem.* 752 (2014) 44–58.
- [59] R.R. Schrock, *Acc. Chem. Res.* 38 (2005) 955–962.